Modeling experiments on seasonal lake ice mass and energy balance in Qinghai-Tibet Plateau: A case study

Wenfeng Huang[1,2], Bin Cheng[3], Jinrong Zhang[1,2], Zheng Zhang[1,2], Timo Vihma[3], Zhijun Li[4,5], Fujun Niu[5]

[1] Key Laboratory of Subsurface Hydrology and Ecological Effects in Arid Region (the Ministry of Education), Chang'an University, Xi'an 710054, China

[2] School of Environmental Science and Engineering, Chang'an University, Xi'an 710054, China

[3] Finnish Meteorological Institute, Helsinki, Finland

[4] State Key Laboratory of Coastal and Offshore Engineering, Dalian University of Technology, Dalian 116024, China

[5] State Key Laboratory of Frozen Soil Engineering, Northwest Institute of Eco-Environment and Resources, Chinses Academy of Sciences, Lanzhou 730000, China

Correspondence to: Wenfeng Huang (huangwenfeng@chd.edu.cn)

Abstract. The lake-rich Qinghai-Tibet Plateau (QTP) has significant impacts on regional and global water cycles and monsoon systems through heat and water vapor exchange. The lake-atmosphere interactions have been quantified over open-water periods, yet little is known about the lake ice thermodynamics and heat and mass balance during the ice-covered season due to a lack of field data. In this study, a high-resolution thermodynamic ice model was applied in experiments of lake ice evolution and energy balance of a shallow lake in QTP. Basal growth and melt dominated the seasonal evolution of lake ice, but also surface sublimation was crucial for ice loss, accounting for up to 40% of the maximum ice thickness. Sublimation was also responsible for 41% of the lake water loss during the ice-covered period. Simulation results matched the observations well with respect to ice mass balance components, ice thickness, and ice temperature. Strong solar radiation, negative air temperature, low air moisture, and prevailing strong winds were the major driving forces controlling the seasonal ice mass balance. The energy balance was estimated at the ice surface and bottom, and within the ice interior and under-ice water. Particularly, almost all heat fluxes showed significant diurnal variations including incoming, absorbed, and penetrated solar radiation, long-wave radiation, turbulent air-ice heat fluxes, and basal ice-water heat fluxes. The calculated ice surface temperature indicated that the atmospheric boundary layer stratification was consistently stable or neutral throughout the ice-covered period. The turbulent air-ice heat fluxes and the net heat gain by the lake were much lower than those during the open-water period.

1. Introduction

The Qinghai-Tibet Plateau (QTP), characterized by a mean altitude of more than 4000 m above sea level (*asl*) and predominated by a freezing climate, is often referred to as the "Third Pole of the Earth". It harbors thousands of lakes covering a total area of approximately 40,700 km^2 (1.4% of the QTP area) and occupying approximately 50% of lakes located in China (Zhang et al., 2014). The QTP is also a headwater region of major Asian rivers including Yangtze, Yellow, Yarlung Tsangpo (Brahmaputra), Mekong, Salween, and Indus Rivers (Immerzeel et al., 2010). Due to its unique climatic environment (e.g. low air pressure and humidity, intense solar radiation, prevailing strong winds, widespread

permafrost and glaciers, and dense lake/river network), QTP directly affects the regional and global water cycle, monsoon system, and atmospheric circulations (Wu et al., 2015; Li et al., 2016b; Su et al., 2016).

The lakes and ponds in QTP play an crucial role in the surface and subsurface hydrological processes (Pan et al., 2014), moisture and heat budgets (Wang et al., 2015; Li et al., 2016a, c; Wen et al., 2016), regional precipitation (Wen et al., 2015), engineering construction (Niu et al., 2011), and gas emission (Wu et al., 2014). The number and surface area of the lakes varies inter-annually. The variations of size are probably due to warming and degradation of permafrost affected by the climate warming through, e.g. thermokarst (Niu et al., 2011), glacier retreating (Liao et al., 2013), increase of precipitation (Lei et al., 2013; Zhang et al., 2014) and strong surface evaporation.

Despite the harsh climatic conditions and the difficulties in access to these lakes, some field campaigns have been performed during ice-free periods in recent years. An unstable or near-neutral atmospheric boundary layer (ABL) prevails over the QTP lake surface in summer (Wang et al., 2015; Li et al., 2015, 2016c). The turbulent heat fluxes show a strong seasonal variation and lag by 2–3 months behind net solar radiation (Li et al., 2016a; Wen et al., 2016). Heat flux dynamics over lake surface differ remarkably from those over other land surface types (like dry/wet grassland) (Biermann et al., 2014). However, the thermal regimes of lakes in QTP and their impacts on the atmosphere boundary layer and surrounding permafrost during wintertime (ice-covered season) remain unclear. Because of sparse field observations, there is an increasing need of models and parameterizations to better understand the lake-air interaction and lake thermal regime (Kirillin et al., 2017; Wang et al., 2015; Wen et al., 2015).

Generally, the QTP lakes and ponds are ice-covered for 3–7 months, depending on their surface area, altitude, and regional climate (Kropáček et al., 2013). Lake ice thermodynamics (ice thickness and temperature) and phenology (the time of freeze-up and break-up, and the duration of the ice cover) play an important role in lake-air interaction (Li et al., 2016a), lake-effect snowfall (Wright et al., 2013), wintertime lake water quality and ecosystems (Kirillin et al., 2012), gas effluxes (Wu et al., 2014), and on-ice transport and operation. All of these issues highlight the accurate representation of QTP lake ice processes. A few investigations on QTP lake ice have been conducted using field measurements and model simulations. Huang et al. (2012, 2013, 2016) reported the ice processes, interior structure, and thermal property in a small shallow thermokarst lake based on their *in situ* observations, and provided significant insights into lake ice thermodynamics and its role in local heat and vapor fluxes and lake water budget. Further, moderate- to high-resolution remote sensing techniques and products, such as MODIS and ENVISAT-ASAR, have been found to be promising and convenient tools for large-scale QTP lake ice research (Kropáček et al., 2013; Tian et al., 2015).

Thermodynamic modeling is an effective and robust methodology to understand lake ice processes and their relationship with local meteorological and hydrological conditions in polar, boreal and temperate regions (Cheng et al., 2014; Semmler et al., 2012; Yang et al., 2012 and 2013).

In this study, we perform a modeling case study of a shallow lake located in the central QTP. Our objectives are (1) to identify the major driving forces that control the seasonal ice mass balance in QTP thermokarst lakes; (2) to quantify the components of mass and energy balance from the ice surface to bottom; (3) to estimate the lake-atmosphere heat and water vapor fluxes through the entire ice-covered period. To the best of our knowledge, lake ice thermodynamic modeling in QTP has not been carried out before. We expect our work can provide a basis for further in situ measurements and upscaling of lake ice simulations over the QTP.

2. Methodology

2.1 Site description

The Beiluhe Basin is located in high pluvial and alluvial plain of the central QTP, with an elevation of 4500–4600 m *asl* (Fig. 1). The topography is undulating, covered by sparse vegetation and sand dunes. This basin is underlain by continuous permafrost 50-80m thick with the volumetric ice content of 30%–50% (Lin et al., 2017). During years 2004-2014, the annual mean air temperature ranged between −4.1 ℃ and −2.9 ℃, and the annual mean ground temperature between −1.8 ℃ and −0.5 ℃(Lin et al., 2017). The annual mean precipitation ranged from 229 to 467 mm (average: 353 mm), while the annual mean potential evaporation ranged from 1588 to 1626 mm (average: 1613 mm) (Lin et al., 2017). There are more than 1200 lakes and ponds with the surface area larger than 1000 m^2 in the Beiluhe Basin. Lake depths are typically 0.5–2.5 m and the shapes are elliptical or elongated.

Lake BLH-A (unofficial name) is located at 34°49.5′N, 92°55.4′E in Beiluhe Basin 4,600 m above sea level. The lake is perennially closed without rivers or streams flowing into and out of it. The minimum and maximum horizontal dimensions of the lake are 120 m and 150 m, respectively, making a total surface area of about 15,000 m^2. The maximum depth is 2.5 m. The water is brackish and has a total dissolved solid of 1.30 g L^{-1}. The lake has been investigated using in situ instrumentation and numerical modeling with respect to lake ice physics (Huang et al., 2011, 2016), hydrothermal regime (Lin et al., 2011), bank retrogression (Niu et al., 2011), and heat intrusion from the lake water to surrounding permafrost (Lin et al., 2017). Considering physical properties of lake ice, a large number of gas bubbles have been found from the top layer of the ice cover. The large gas content caused a small bulk ice density (880–910 kg m^{-3}) and a small thermal conductivity (1.60–2.10 W m^{-1} K^{-1})) (Huang et al., 2012, 2013; Shi et al., 2014).

2.2 Field observations

Field campaigns were conducted in Lake BLH-A through three consecutive winters from 2010–2011 to 2012–2013, to record the ice-water-sediment temperatures (T_i, T_w, and T_{sed}), air temperature (T_a), and surface and bottom growth and decay of the ice cover. A floater was designed and deployed onto the water surface (Fig. 1). A thermistor cable was fixed to the floater to measure the ice-water temperature at 5 cm interval. An upward-looking ultrasonic sensor was also fixed to the floater and positioned at 100 cm depth to monitor depth of the ice-water interface. A downward-looking ultrasonic sensor was fixed to a steel pipe, which had been inserted into the lake sediment by ~60 m, to monitor the position/depth of ice surface. All measures were recorded every 30 min through the whole ice season. The data yielded the following information: the dates of freeze-up and break-up (D_f and D_b) and time series of the vertical positions of (a) the ice-water interface (H_b), representing the basal melt or growth, and (b) the air-ice interface (H_s), representing the surface sublimation or/and melting. Hence, the evolution of ice thickness ($H = H_b − H_s$) was detected. For detailed information on instrumentation, see Huang et al. (2016).

The Beiluhe weather station (BWS), located 800 m southeast from the lake, monitored the air temperature (T_a), air relative humidity (Rh), atmospheric pressure (P_a), water vapor pressure in the air (e_a), wind speed (V_a) and direction, incident short- and long-wave irradiance (Q_l and Q_s) at 2 m and 10 m above the ground surface, and accumulated precipitation (water equivalent, $Prec$). In this paper we focus on the ice season of 2010–2011, when the observed datasets have the highest quality and least

126 missing values. Furthermore, the data reveal a typical seasonal cycle of the lake ice phenology (Fig. 2).

127 In early freezing season in late October, a thin ice layer typically formed at nights and melted during
128 daytime. Finally, a stable ice cover formed in early November (freeze-up). A strong surface sublimation
129 process at the ice-air interface was observed through the whole ice season, reducing the total ice
130 thickness congealed from the ice-water interface. The absolute thickness reached its maximum (~ 60
131 cm) in early February. On the basis of our field visits during freezing (early December) and melting
132 (late March) stages and the constant low temperature and strong wind through the ice season, we
133 concluded that the bare ice surface was most probably persistently dry without melt water throughout
134 the 2010–2011 ice season.

135 **2.3 Thermodynamic snow and ice model**

136 A well calibrated (Launiainen and Cheng, 1998, Vihma et al., 2002) and widely used (Cheng et al.,
137 2006, 2008; Semmler et al., 2012; Yang et al., 2012 and 2013; Cheng et al., 2014) thermodynamic
138 snow and ice model (HIGHTSI) is applied in this study to investigate Lake BLH surface energy and ice
139 mass balances. The surface heat balance reads:

140 $$(1 - \alpha)(1 - \gamma)Q_s + Q_l + \varepsilon\sigma T_s^4 + Q_{le} + Q_h + Q_p + F_c = F_m \quad (1)$$

141 where Q_s and Q_l is the incident shortwave and longwave radiation, respectively, α is the surface albedo,
142 γ is the fraction of solar radiation penetrating the surface, ε is the thermal emissivity of the surface
143 (ice/snow), σ is the Stefan-Boltzmann constant, T_s is the surface temperature, Q_{le} and Q_h are the latent
144 and sensible heat fluxes, Q_p is the heat flux from precipitation, which can be neglected in QTP during
145 wintertime, F_c is the conductive heat flux in the ice at the surface, and F_m is the surface heat balance.
146 Heat flux towards the ice surface was defined positive. Surface melting is accordingly calculated as:

147 $$\rho_i L_f \frac{dH}{dt} + F_m = k_{iup} \frac{\partial T}{\partial z} \quad (2)$$

148 where ρ_i is the ice density, L_f is the latent heat of freezing, k_{iup} is the thermal conductivity of ice at
149 upper ice layer, T is the ice temperature, and z is the vertical coordinate. The incident short- and
150 longwave radiative fluxes are either parameterized, taking into account cloudiness, or prescribed by
151 observations or NWP model output. The penetration of solar radiation into the snow and ice is
152 parameterized according to surface albedo and optical properties of snow and ice. The turbulent heat
153 fluxes (Q_e and Q_c) at ice-air interface are parameterized using the bulk-aerodynamic formulae as
154 follows:

155 $$Q_{le} = \rho_a L C_e V_a (q_s - q_a) \quad (3)$$
156 $$Q_h = \rho_a c_p C_h V_a (T_s - T_a) \quad (4)$$

157 where ρ_a is the air density, L is the latent heat of sublimation of ice when $T_s < 0$ ℃ or of evaporation of
158 water when $T_s \geq 0$ ℃, V_a is the wind speed at the reference height (2.0 m), T_s is the ice surface
159 temperature, q_s is the saturation specific humidity corresponding to T_s, and q_a and T_a are the specific
160 humidity and temperature of air at the reference height, and C_e and C_h are the bulk transfer coefficients
161 for heat and water vapor, respectively. Both transfer coefficients are parameterized taking into account
162 the thermal stratification of the atmospheric boundary layer (Launiainen and Cheng, 1998; Wang et al.,
163 2015). In addition, Q_{le}/L gives the equivalent thickness of sublimated ice or of evaporated water E.

164 $$E = \frac{Q_{le}}{L} \quad (5)$$

165 Within the ice column, a sophisticated two-layer radiative transfer model is used taking into account
166 a thin surface layer that is different from the ice layer below with respect to optical properties (Maykut

167   and Perovich, 1987).

168   At the bottom boundary, the ice growth/melt is calculated on the basis of the difference between the

169   heat flux from lake water to ice base (F_w) and the conductive heat flux at the ice bottom layer:

170   $$\rho_i L_f \frac{dH}{dt} + F_w = k_{idn} \frac{\partial T}{\partial z} \qquad (6)$$

171   where k_{idn} is the thermal conductivity of ice at ice bottom layer. In HIGHTSI, F_w is either prescribed as

172   a constant value or prescribed based on in situ observations.

173   The evolutions of thickness and temperature of snow and ice are obtained by solving the heat

174   conduction equations for multiple ice and snow layers. Eq (1) solves the surface temperature, which is

175   used as the upper boundary condition as well as to determine whether surface melting occurs. The ice

176   bottom temperature keeps at the freezing point.

177   **2.4 Meteorological data and model parameters**

178   The meteorological data are based on the BWS (Fig. 3). The 2-m air temperatures observed on the lake

179   site were highly correlated with the measurement at BWS station with averaged difference of 0.3 ℃

180   ($R^2 = 0.98$). The T_a has a strong diurnal cycle in response to the large diurnal cycle of solar radiation.

181   The mean T_a was -10.6 ℃ during simulation period from 9 November, 2010, to 25 April, 2011. The

182   northwest winds prevailed during the winter season. The gust wind speed was frequently stronger than

183   10 m/s. The average wind speed was 6.5 m s^{-1} associated with an average relative humidity of 34 %

184   only.

185   The daily insolation lasted for 10-12 hours and the average daily (24 h) solar radiation Qs was about

186   390 W m^{-2} during the simulation period, with the daily maximum ranging from 570 to 1140 W m^{-2}. The

187   averaged downward longwave radiation during daytime (8:00-19:00, local time) and nighttime

188   (19:00-8:00) was approximately 177 and 180 W m^{-2}, respectively. The radiative cooling due to negative

189   net radiation was strong during nighttime.

190   The snow pack was very thin, literally zero, during winter 2010–2011. There were a few minor

191   snowfall events, but no snow accumulation because of strong wind. A major detectable snowfall

192   occurred in early April (~ 9 cm of snow), but the snow was blown off in a short time. For simplicity,

193   snow was not taken into account in the model simulation. The transparent ice allowed solar radiation to

194   penetrate into the ice interior and further down to the under-ice water column, heating the ice/water

195   column daily.

196   The sky was persistently clear over the whole ice season 2010–2011. High cloudiness and overcast

197   conditions occurred only during late ice season. A slight thin film of fine sand accumulated on the ice

198   surface in early spring coloring the ice surface light yellow. The surface albedo may have accordingly

199   reduced, leading more solar radiation absorption at and below the surface. An albedo parameterization

200   scheme for a climate system model developed by Briegleb et al., (2004) was applied in this study, but

201   the impact of the surface dust film was not taken into consideration.

202   When running the HIGHTSI model, we have to input values of the heat flux F_w. which is

203   challenging to be observed. Actually, we estimate F_w using heat residual method at ice base based on *in*

204   *situ* measurements of in-ice temperature profile and the rate of basal ice growth (Huang et al., 2019).

205   But for a reference run, a prescribed time series for the derived F_w was used. The average F_w was

206   approximated 27 W m^{-2}.

207   For the reference run, model forcing data and parameters are given in Table 1.

208   **3. Results and analysis**

209   **3.1 Lake ice thickness and mass balance**

210   The BLH-A lake ice congelation lasted from early November to the beginning of February. Through
211   February, the ice growth reached a thermal equilibrium stage, and the ice thickness did not change
212   much. From the beginning of March, the ice started to melt, most at the ice bottom and also within the
213   ice interior. Finally, the ice cover disappeared at the end of April. The growth, thermal equilibrium, and
214   melting periods lasted for approximately 87, 30, and 56 days, respectively.

215   The lake ice mass balance consists of the surface ice sublimation and melting, bottom freezing and
216   melting (Fig. 4a). The ice bottom evolution (congelation ice) dominated the ice growth to 0.75 m until
217   day 430 before a melting started at the ice bottom. The model calculated a total surface melting (~0.12
218   m) at the end of the ice season. A strong loss of latent heat flux during the entire period generated some
219   0.23 m of lake ice sublimation at the ice surface. The observed air-ice interface evolution (Fig. 2)
220   revealed the integrated impacts of surface sublimation and melting (during the late season), which
221   could not be instrumentally delineated from each other. By regrouping the modeled ice mass balance
222   components, we can calculate the evolution of the ice surface (i.e. surface sublimation + melting) and
223   ice bottom, and compare them with the measurements (Fig. 4b). Although the modeled ice bottom
224   depth is 4.2 cm larger than measured one (Table 2), the HIGHTSI model very well captured the general
225   evolution both at the ice surface and bottom. The modeled total ice thickness (i.e. $Depth_B - Depth_S$) is in
226   good agreement with the observations (Fig. 4c). However, during day 460, the ice melting was stopped
227   due to a snowfall event. This short-term pause was not revealed by the model since the snow thickness
228   was assumed zero.

229   HIGHTSI modeling also affirmed that there are obvious and strong diurnal cycles of freezing and
230   melting at the ice bottom when the ice thickness is less than ~ 20 cm, especially in late spring. For
231   instance, during the melting stage, the ice melts rapidly from 9:00-10:00 to 17:00-18:00, and undergoes
232   an equilibrium or minor growth from 18:00 to 6:00-8:00, then melts again during daytime at the bottom.
233   Besides, the model also detected diurnal variations in the surface sublimation and melting.

234   Statistical analysis indicated that the model results and measurements for ice mass balance have a
235   high correlation (R > 0.97) and small standard deviations (< 3.6 cm), and match very well in terms of
236   surface and bottom depth evolutions and ice thickness with *MAEs* and *RMSEs* generally lower than 5.5
237   cm (Table 2).

238   **3.2 Lake ice temperatures**

239   The modeled ice temperature regime (Fig. 5) revealed that there are strong diurnal cycles in ice
240   temperature throughout the ice season, following the large diurnal cycle in air temperature and solar
241   radiation. This is consistent with the observed ice thermal dynamics. The calculated surface
242   temperature of ice was continuously lower than the freezing point, except during daytime in late April,
243   when it revealed some cycles of daytime melting and nighttime freezing at the surface.

244   The calculated and observed vertical profiles of ice temperature were compared at selected time
245   steps (Fig. 6). The ice temperature was modeled quite well during the ice growth period (Figs. 6a-d).
246   During the equilibrium and melting stages, the observed and modeled temperature discrepancies were
247   larger especially at the surface and bottom parts. This could have resulted from several processes. From
248   the beginning of the equilibrium stage, the solar radiation increased gradually and was absorbed by the

thermistor sensors at top layer, leading to higher observed values near the surface during daytime (Fig. 6e). During the melting period, the bottommost part of the ice column underwent fast phase change, and the inter-crystal spaces could be filled with underlying warm water. The sensors near the ice bottom actually detected the integrated temperature of ice and water, thus the observed temperature could be quite close to and even slightly higher than the freezing point (0 ℃) (Figs. 6e,f). On the other hand, the linearly interpolated surface depth is likely to cause errors in determining the true sensor depths within the sublimating ice cover, causing some temperature differences.

3.3 Modeled Energy balance

The lake ice thickening and thinning and temperature regime (i.e. phase transitions) are governed by the energy transport and translation through the air-ice-water column. The good performances of HIGHTSI model in calculating the ice mass balance and temperature dynamics argue comprehensive estimates of heat/radiation transfer and partitioning within the air-ice-water column. For a seasonal cycle, the monthly means of various heat fluxes were calculated at the ice surface, within the ice interior, and at the ice bottom (Table 3).

The net shortwave radiation (Q_{sn}) absorbed by the lake acted as a main energy source for ice and water thermodynamics, and followed the seasonal variation of total incident solar radiation (Q_s). The Q_{sn} penetrated through the ice surface and interior, and into the under-ice water column. Therefore, it was divided into three parts: the net solar radiation used for surface energy balance ($Q_{ss}=(1-\alpha)(1-\gamma)Q_s$) (~43% of Q_{sn}), the absorption by the ice interior beneath surface (Q_{si}) (~36%), and the absorption by water (Q_{sw}) (~21%), all of which also showed similar seasonal variation to Q_s. The water heat flux into ice (F_w) that represents the temperature difference between the water and ice bottom, was larger when the ice was thinner. The turbulent heat fluxes did not show strong seasonal variations through the ice season. Furthermore, almost all of the heat fluxes showed strong diurnal variations (Fig. 7). All radiative fluxes (Q_s, Q_{sn}, Q_{si}, and Q_{sw}) had synchronous diurnal cycles, peaked at noon and disappeared through night. The sensible heat flux (Q_h) peaked in the afternoon and had its minimum just before the dawn. The latent heat flux (Q_{le}) had an opposite diurnal pattern with a minimum in the afternoon and maximum in the early morning. The net longwave radiation (Q_{ln}) and surface conductive heat flux (F_c) had roughly opposite diurnal cycles with extremes at midnight.

For the thin surface layer, the upward conductive heat flux (F_c) represents the near surface ice temperature gradient. When the ice was thin (e.g. in November), the larger F_c indicates more heat lost from the ice bottom to surface, and thus rapid ice growth. The net long-wave radiation ($Q_{ln}=Q_l-\varepsilon\sigma T_s^4$) was consistently negative and indicated that the ice surface emitted the heat back to the air/space all the time. The sensible heat flux (Q_h) was generally positive, thus argued heat gain from the air. The large negative latent heat flux (Q_{le}) (Table 3) manifested that the surface sublimation was strong (Fig. 4a). According to the surface heat balance (Eq. 1), the residual F_m was close to zero, indicating a dry cold surface. However, in April, its positive value revealed that the ice melted at surface (Fig. 4a), and the latent heat was induced by evaporation of meltwater during late melting season instead of sublimation of ice.

Within the ice interior, the absorbed solar radiation Q_{si} was used to heat the ice during daytime and thus caused the diurnal variation in ice temperature (Fig. 5), and also led to interior melt in a manner of gas pore expansion during the late ice season (Leppäranta et al., 2010).

Beneath the ice bottom, the under-ice water column absorbed the transmitted solar radiation Q_{sw} and raised its temperature at daytime. According to the lake sediment temperature measurements in BLH-A

by Lin et al. (2011, 2017), through the whole ice-covered season the bottom sediment releases quite limited heat to lake water ($- 0.2 \sim -0.6$ W m^{-2}), consequently, this heat flux can be ignored. For the energy balance of under-ice water, the penetrated solar radiation is the pivotal heat source, of which 56% is released into the ice bottom (F_w), 44% is used to increase the bulk water temperature and partly is transformed to turbulent kinetic energy forcing water convection, and few ($< 0.1\%$) is transported to bottom sediment (permafrost and talik).

3.4 Model experiment on F_w

Usually, the water-to-ice heat flux F_w is assumed to be constant throughout an ice season when simulating ice thickness in Arctic or temperate lakes. Therefore, under the same weather forcing condition, a number of model experiments have been performed using a constant F_w (ranging from 0 to 50 W m^{-2} with an interval of 5 W m^{-2}).

During the modeling period, the average ice growth at bottom was 0.49 m with a maximum of about 0.72 m. The average and maximum ice thicknesses were 0.38 m and 0.61 m, respectively. Model experiments indicated that the average F_w cannot be smaller than 15 W m^{-2} because otherwise both average and maximum ice thicknesses would differ a lot from observations (Fig. 8). If average F_w is about 35 W m^{-2}, the modeled average and maximum net total ice thickness are not far from the observed values, but have large offsets at ice bottom, especially for the maximum ice growth at ice bottom. If average F_w is more than 35 W m^{-2}, the errors for both average and maximum ice thicknesses are getting larger. It seems when average F_w is between 20 W m^{-2} and 30 W m^{-2}, the modeled results are within the ranges of observed values with respect to total and bottom growth ice thicknesses.

In reality, F_w is not a constant value. Model experiments argued that the mass balance at ice base cannot be reproduced using constant F_w through the whole ice season. Based on heat residual method, we created the time series of F_w (Fig. 9) to carry out the reference run (Fig. 4) that gave a very good agreement to the observations.

Different from the ocean and large deep lake, where the variation of F_w is largely driven by the under-ice currents (Krishfield and Perovich, 2005; Rizk et al., 2014), BLH-A is very shallow and the water below ice is largely at a standstill, so the driving force for F_w most likely is the penetrated solar radiation. The modeled solar radiative flux that penetrates through the ice layer and reaches at ice bottom is plotted in Fig. 9. In early simulation, ice was very thin and the surface albedo is small, so large part of solar radiation penetrated through ice layer and warmed the underlying water, creating a large F_w. When ice was getting thicker, the surface albedo increased and the penetrated solar radiation was reduced. In later part of the season, melting of ice reduced the surface albedo, the downward solar radiation was simultaneously increased, and more solar radiation was accordingly absorbed in the lake water below the ice. The average solar radiation absorbed by the under-ice water column during the entire simulation period was 22 W m^{-2}. Additionally, the heat flux induced by changes in underlying water temperature (i.e. heat content in water) was estimated to be 3 W m^{-2}. The total 25 W m^{-2} is in the range of good agreement between observed and modeled ice thickness (Fig. 8).

4. Discussion

4.1 Implication on ABL over ice-covered lakes

The characteristics of the ABL play a direct role in the turbulent heat and mass fluxes. The modeled

and observed temperature profiles through the air-ice-water column presented here can give a close insight into the features of the ABL over the lake during the ice-covered period taking the temperature difference between the lake (ice) surface and the air as a bulk stability indicator. The ice surface temperature (T_s) was generally lower than the air temperature (T_a). The monthly mean T_s was consistently lower than the monthly T_a by 1.24 ± 0.55 °C from December through April, indicating a persistent stable ABL through the ice-covered period (Fig. 10). However, the T_s was 0.31 °C higher than T_a in November when the ice was rapidly growing, especially when the ice thickness was less than ~ 10 cm (i.e., before Nov. 20).

Previous investigations revealed that the QTP lakes are predominantly characterized by unstable ABL during open-water period (Li et al., 2015; Wang et al., 2015; Wen et al., 2016). The present results indicated that the ABL over lake turns into a stable or neutral stratification soon after the lake ice forms. When the lake ice disappears, the ABL soon turns into an unstable straitification again (Wen et al., 2016). However, short-term periods of unstable ABL were observed for approximately 25% of the ice duration period. The unstable conditions usually took up on diurnal scale especially following sudden drops of the air temperature.

4.2 The air-lake heat exchange

Diurnal changes in turbulent heat fluxes, however, are large and are commonly seen in high-latitude and high-altitude lakes (e.g. Vesala et al., 2006; Rouse et al., 2008; Nordbo et al., 2011; Wang et al. 2015; Li et al. 2016a, c; Wen et al. 2016). In our study, the mean values of turbulent heat fluxes of Q_h and Q_{le} were 14 W m^{-2} and −41 W m^{-2}, respectively. These numbers are in line with observations that were obtained in QTP lakes in winter season (Li et al., 2016a). At seasonal scale, the Q_h and Q_{le} over lake ice are approximately 40%−60% lower than values during ice-free seasons, demonstrating the role of ice as an insulator. The present turbulent heat fluxes are somewhat larger than those observed at Great Slave Lake (Blanken et al., 2000) and a boreal lake in south Finland (Nordbo et al., 2011) during the open-water period. This is attributed to the stronger wind and drier air prevailing over the QTP.

The net heat exchange ($Q_{net}= Q_{sn} +Q_{ln}+Q_h+Q_{le}$) through the atmosphere-lake interface showed strong diurnal and seasonal cycles. Q_{net} increased gradually through the whole ice season. The lake ice released heat into the atmosphere until early March, and then gained heat from the atmosphere. Integrated over the ice season, the lake released heat of about 266 MJ m^{-2} (i.e. ~17 W m^{-2}).

4.3 Water vapor flux and lake water balance

The water balance in a lake reads

$$\Delta V = P - E + R_s + R_g \qquad (7)$$

where ΔV is the lake water change, and P, E, R_s and R_g are the precipitation, evaporation, net surface inflow and subsurface inflow, respectively.

During the freezing season in central QTP, the precipitation is generally quite small and the surface inflow and outflow through gullies and streams are typically blocked due to the freezing conditions. Therefore, the lake water balance is strongly affected by evaporation/sublimation and subsurface inflow/outflow.

Assuming ice density of 900 kg m^{-3}, the modeled sublimated ice thickness E can be converted to water equivalent (WE) (Fig. 12). The monthly mean sublimation was the weakest in December and January, but higher in February and March. This is probably due to the stronger winds and higher ice

373 surface temperature; the latter was favored by more incident long- and short-wave radiation than before.
374 Through the entire ice season, the ice surface water loss due to evaporation/sublimation was
375 approximately 207 mm *WE*.
376   The BLH-A lake water level observations revealed a decrease of 0.50 m through the entire ice season
377 (Lin et al., 2017). The surface evaporation/sublimation hence accounts for 41% of lake water loss
378 during the ice-covered period and for 42% of annual water loss (Pan et al., 2017). The remaining part
379 of water loss is probably caused by vertical percolation through the lake sediment to supply deep
380 groundwater, since the talik (a layer of year-round unfrozen ground) beneath the lake has developed
381 through the underlying permafrost (Lin et al., 2011, 2017; Niu et al., 2011), and by the lateral water
382 discharge into ambient soil during the thickening and thinning of frozen active layer (Pan et al., 2017;
383 Lin et al., 2017). But over the entire hydrological year, the lake water loss through subsurface discharge
384 and evaporation/sublimation is roughly offset by the heavy precipitation, surface runoff, and
385 supra-permafrost recharge during warm seasons (Lei et al., 2017; Pan et al., 2017). Therefore, the
386 studied lake level is nearly stabilized inter-annually (Lin et al. 2017; Gao et al., 2018).

387 **5. Summary and conclusions**

388 The ice season was characterized by a freezing period (9 November – 4 February), a thermal
389 equilibrium period (5 February –10 March), and a melting period (11 March – 30 April). During the
390 freezing period, strong atmospheric cooling caused a growth of congelation ice of about 70 cm. The
391 major driving force for ice growth was a consistent subzero air temperature (mean -13 ℃) and a strong
392 average net longwave radiative cooling (-97 W m^{-2}), although the ice surface absorbed a net solar
393 radiative flux of 77 W m^{-2} on the average.
394   During melting period, the ice melt rate was about 14 mm/day. Basal melting dominated and surface
395 melting was only seen by the very end of the ice season, because air temperatures remained subzero
396 during most of the winter. A total 0.23 m of ice thickness was lost at the surface due to a sustained
397 sublimation process during the entire study period. This was caused by a combined effect of prevailing
398 strong winds and dry air. The observed average wind speed and relative humidity were 7 m s^{-1} and 34%,
399 respectively.
400   Comparisons with an Arctic lake revealed the uniqueness of QTP lakes especially with respect to the
401 atmospheric forcing, lake geometry, ice cover (free of snow), and under-ice hydro-thermodynamics
402 (Table 4). These features challenge the existing lake ice models that are mainly developed for Arctic
403 and temperate regions. However, present modeling experiments indicated that HIGHTSI could yield
404 reasonable results in terms of the surface and bottom freezing/ablation and ice thermodynamics.
405   Additionally, HIGHTSI results indicated that the net long-wave radiative cooling (-97 W m^{-2}) and
406 upward conductive heat flux in the ice interior as well as turbulent latent heat flux dominated the ice
407 surface energy and mass balance. The average net solar radiative flux was large (181 W m^{-2}); 40% of it
408 was reflected back to the space, 34% was absorbed below the ice surface, and only 26% was used for
409 surface energy balance. Diurnal cycles of surface heat fluxes were driven by the diurnal variations of
410 shortwave radiation. The observed air temperature and calculated ice surface temperature suggested a
411 consistent stably stratified ABL during most of the ice-covered period, except when the ice thickness
412 was less than ~10 cm. Averaged over the entire ice-covered season, the lake (ice) released 17 W m^{-2}
413 heat to the atmosphere.
414   The ice surface mass balance was dominated by surface ice sublimation, which was modeled very

well. The sublimation was demonstrated to be a key component for lake water balance and accounted for 41% of lake water loss during wintertime. In light of the generally low air humidity and strong wind over QTP, the sublimation can be critical for the water balance of a large number of shallow lakes and ponds over the QTP, and further research (observations and modelling) is needed for quantification of sublimation in a regional scale over QTP.

The water-ice heat flux F_w controlled the basal, and thus, the net ice thickness evolution. The model experiments indicated that constant F_w through the whole ice season cannot produce a reasonable basal mass balance. A parameterized time series of F_w was used and yielded realistic results. This confirmed the temporal variation in F_w in shallow QTP thermokarst lakes. Many more observations should be made to quantify F_w and better understand the physics governing it.

The present modeling experiments indicated that the largest uncertainty for QTP lake ice modeling is the effect of F_w. Thermokarst lakes on QTP are typically shallow and small, without significant surface water input and output, implying that through-lake current or lake-wide circulation under the ice cover are negligible (Kirillin et al., 2015). Cold sediment layer limits the heat release into the overlying water (Lin et al., 2011). However, the solar radiation is strong (due to persistent clear-sky conditions), and the lake ice cover is consistently free of snow. In QTP, the surface albedo of ice in large deep lakes can be unprecedentedly small (<0.2) (Li et al., 2018). Indeed, in our study the Briegleb albedo scheme yielded a small albedo, in particular, when the ice was thin. Intensive penetrative solar radiation can drive under-ice turbulent mixing of mass and heat (Mironov et al., 2002). However, the quantitative effects of penetration of solar radiation on F_w are not yet well known, and new field experiments are needed.

Snow was neglected in this modeling work. However, snowfall occasionally occurs on QTP, and may have a strong impact in ice mass balance, especially for large lakes (Cheng et al., 2014). The major impact of snow on ice thermodynamics is the insulation effect (Leppäranta, 2015). Snow-ice is not likely to form on QTP, since in early winter the air temperature drops fast and the ice freezes quickly. However, superimposed ice may be formed in late spring, if there is thick snow on top of ice. Otherwise, snow can compensate the strong ice mass loss due to sublimation, decreasing the water loss in QTP lakes in winters.

Data availability. The datasets on lake ice temperatures and thickness, and meteorological forcing used for modeling and comparison can be downloaded from https://www.researchgate.net/publication/329826495_QTP_lake_ice_and_meteorology_data. Model code and results are available from the first (huangwenfeng@chd.edu.cn) and second author (Bin.Cheng@fmi.fi) by request.

Competing interests. The authors declare no competing interests.

Acknowledgements. This work is supported by the National Natural Science Foundation of China (41402203, 51579028), the Natural Science Fund of Shaanxi Province (2018JQ4021), the Special Fund for Basic Scientific Research of Central Colleges (310829171002, 310829161006), and the Open Fund of State Key Laboratory of Frozen Soils Engineering (SKLFSE201604). We are also grateful to the staff from the Field Station of Permafrost Engineering and Environmental Tests for their field assistance, and PEEX program for providing international cooperation.

References

Biermann, T., Babel, W., Ma, W., Chen, X., Thiem, E., Ma. Y., and Foken, T.: Turbulent flux observations and modeling over a shallow lake and a wet grassland in the Nam Co basin, Tibetan Plateau, Theor. Appl. Climatol., 116, 301-316, 2014.

Blanken, P.D., Rouse, W.R., Culf, A.D., Spence, C., Boudreau, L.D., Jasper, J.N., Kochtubajda, B., Schertzer, W.M., Marsh, P., and Verseghy, D.: Eddy covariance measurements of evaporation from Great Slave Lake, Northwest Territories, Canada, Water Res. Res., 36(4), 1069-1077, 2000.

Briegleb, B., Bitz, C.M., Hunke, E.C., Lipscomb, W.H., Holland, M.M., Schramm, J., and Moritz, R.: Scientific description of the sea ice component in the Community Climate System Model, Ver. 3, NCAR/TN-463+STR, NCAR Tech Note, 1-78, 2004.

Cheng, B., Vihma, T., Rontu, L., Kontu, A.: Evolution of snow and ice temperature, thickness and energy balance in Lake Orajärvi, northern Finland, Tellus A, 66, 21564, http://dx.doi.org/10.3402/tellusa.v66.21564, 2014.

Cheng, B., Vihma, T., Pirazzini, R., and Granskog, M.: Modeling of superimposed ice formation during spring snowmelt period in the Baltic Sea, Ann. Glaciol., 44, 139–146, 2006.

Cheng, B., Zhang, Z., Vihma, T., Johansson, M., Bian, L., Li, Z., and Wu, H.: Model experiments on snow and ice thermodynamics in the Arctic Ocean with CHINARE 2003 data, J. Geophys. Res., 113, C09020, doi:10.1029/2007JC004654, 2008.

Huang, W., Han, H., Shi, L., Niu, F., Deng, Y., and Li, Z.: Effective thermal conductivity of thermokarst lake in Beiluhe Basin, Qinghai-Tibet Plateau, Cold Reg. Sci. Technol., 85, 34-41, 2013.

Huang, W., Li, R., Han, H., Niu, F., Wu, Q., and Wang, W.: Ice processes and surface ablation in a shallow thermokarst lake in the central Qinghai-Tibet Plateau, Ann. Glaciol., 57(71), 20-28, 2016.

Huang, W., Li, Z., Han, H., Niu, F., Lin, Z., and Leppäranta, M.: Structural analysis of thermokarst lake ice in Beiluhe Basin, Qinghai-Tibet Plateau, Cold Reg. Sci. Technol., 72, 33-42, 2012.

Huang, W., Zhang, J., Leppäranta, M., Li, Z., Cheng, B., and Lin, Z.: Thermal structure and water-ice heat transfer in a shallow ice-covered thermokarst lake in central Qinghai-Tibet Plateau, to be submitted, 2019.

Immerzeel, W.W., van Beek, L.P.H., and Bierkens, M.F.P.: Climate change will affect the Asian water towers, Science, 328, 1382-1385, 2010.

Jonas, T., Terzhevik, A.Y., Mironov, D.V., and Wüest, A.: Radiatively driven convection in an ice-covered lake investigated by using temperature microstructure technique, J. Geophys. Res., 108(C6), 3183, doi: 10.1029/2002JC001316, 2003.

Kirillin, G.B., Forrest, A.L. Graves, K.E., Fischer, A., Engelhardt, C., and Laval, B.E.: Axisymmetric circulation driven by marginal heating in ice-covered lakes, Geophys. Res. Lett., 42, 2893-2900, 2015.

Kirillin, G., Leppäranta, M., Terzhevik, A., Granin, N., Bernhardt, J., Engelhardt, C., Efremova, T., Golosov, S., Palshin, N., Sherstyankin, P., Zdorovennova, G., and Zdorovennov, R.: Physics of seasonally ice-covered lakes: a review, Aquat. Sci., 74(4), 659-682, 2012.

Kirillin, G., Wen, L., and Shatwell, T.: Seasonal thermal regime and climatic trends in lakes of the Tibetan Highlands, Hydrol. Earth Syst. Sci., 21, 1895-1909, 2017.

Krishfield, R.A., and Perovich, D.K.: Spatial and temporal variability of oceanic heat flux to the Arctic ice pack, J. Geophys. Res., 110, C07021, doi: 10.1029/2004JC002293, 2005.

Kropáček, J., Maussion, F., Chen, F., Hoerz, S., and Hochschild, V.: Analysis of ice phenology of lakes on the Tibetan Plateau from MODIS data, The Cryosphere, 7, 287-301, 2013.

Launiainen, J., and Cheng, B.: Modeling of ice thermodynamics in natural water bodies, Cold Reg. Sci. Technol., 27(3), 13-178, 1998.

Lei, Y., Yao, T., Yang, K., Sheng, Y., Kleinherenbrink, M., Yi, S., Bird, B. W., Zhang, X., Zhu, L., and Zhang. G.: Lake seasonality across the Tibet Plateau and their varying relationship with regional mass balance and local hydrology, Geophys. Res. Lett., 44, 892-900, doi: 10.1002/2016GL072062, 2017.

Lei, Y., Yao, T., Bird, B. W., Yang, K., Zhai, J., and Sheng, Y.: Coherent lake growth on the central Tibetan Plateau since the 1970s: Characterization and attribution, J. Hydrol., 483(3), 61-67, 2013.

Leppäranta, M.: Freezing of lakes and the evolution of their ice cover, Springer, Berlin, Heidelberg, 2015.

Leppäranta, M., Terzhevik, A., and Shirasawa, K.: Solar radiation and ice melting in Lake Vendyurskoe, Russian, Hydrol. Res., 41(1), 50-62, 2010.

Li, X., Ma, Y., Huang, Y., Hu, X., Wu, X., Wang, P., Li, G., Zhang, S., Wu, H., Jiang, Z., Cui, B., and Liu, L.: Evaporation and surface energy budget over the largest high-altitude saline lake on the Qinghai-Tibet Plateau, J. Geophys. Res.- Atmos., 121(18), 10470-10485, 2016a.

Li, Y., Zhang, C., and Wang, Y.: The verification of millennial-scale monsoon water vapor transport channel in northwest China, J. Hydrol., 536, 273-283, 2016b.

Li, Z., Ao, Y., Lyu, S., Lang, J., Wen, L., Stepanenko, V., Meng, X., and Zhao, L.: Investigations of the ice surface albedo in the Tibetan Plateau lakes based on the field observation and MODIS products, J. Glaciol., doi: 10.1017/jog.2018.35, 2018.

Li, Z., Lyu, S., Zhao, L., Wen, L., Ao, Y., and Wang, S.: Turbulent transfer coefficient and roughness length in a high-altitude lake, Tibetan Plateau, Theor. Appl. Climatol., 124, 723-735, 2016c.

Li, Z., Lyu, S., Ao, Y., Wen, L., Zhao, L., and Wang, S.: Long-term energy flux and radiation balance observations over Lake Ngoring, Tibetan Plateau, Atmos. Res., 155, 13-25, 2015.

Liao, J., Shen, G., and Li, Y.: Lake variations in response to climate change in the Tibetan Plateau in the past 40 years, Int. J. Digit. Earth, 6(6), 534-549, doi:10.1080/17538947.2012.656290, 2013.

Lin, Z.J., Niu, F.J., Fang, J.H., Luo, J., and Yin, G.A.: Interannual variations in the hydrothermal regime around a thermokarst lake in Beiluhe, Qinghai-Tibet Plateau, Geomorphology, 276, 16-26, 2017.

Lin, Z., Niu, F., Liu, H., and Lu, J.: Hydrothermal processes of alpine tundra lakes, Beiluhe Basin, Qinghai-Tibet Plateau, Cold Reg. Sci. Technol., 65, 446-455, 2011.

Maykut, G. A., and Perovich, D. K., 1987. The role of shortwave radiation in the summer decay of a sea ice cover. J. Geophys. Res. 92(C7), 7032–7044.

Mironov, D., Terzhevik, A., Kirillin, G., Jonas, T., Malm, J. and Farmer, D.: Radiatively driven convection in ice-covered lakes: Observations, scaling, and a mixed layer model, J. Geophys. Res., 107(C4), 3032, doi: 10.1029/2001JC000982, 2002.

Mountain Research Initiative EDW Working Group: Elevation-dependent warming in mountain regions of the world, Nature Clim. Change, 5, 424-430, 2015.

Niu, F., Lin, Z., Liu, H., and Lu, J.: Characteristics of thermokarst lakes and their influence on

543   permafrost in Qinghai-Tibet Plateau, Geomorphology, 132, 222-233, 2011.

544 Nordbo, A., Launiainen, S., Mammarella, I., Leppäranta, M., Houtari, J., Ojala, A., and Vesala, T.:
545   Long-term energy flux measurements and energy balance over a small boreal lake using eddy
546   covariance technique, J. Geophys. Res., 116, D02119, doi: 10.1029/2010JD014542, 2011.

547 Pan, X., Yu, Q., You, Y., Chun, K. P., Shi, X., and Li, Y.: Contribution of supra-permafrost
548   discharge to thermokarst lake water balances on the northeastern Qinghai-Tibet Plateau, J.
549   Hydrol., 555, 621-630, 2017.

550 Rizk, W., Kirillin, G., and Leppäranta, M.: Basin-scale circulation and heat fluxes in ice-covered
551   lakes, Limnol. Oceanogr., 59(2), 445-464, , 2014.

552 Semmler, T., Cheng, B., Yang, Y., and Rontu, L.: Snow and ice on Bear Lake (Alaska)-sensitivity
553   experiments with two lake ice models, Tellus A, 64, 17339, doi:10.3402/tellusa.v64i0.17339,
554   2012.

555 Shi, L., Li, Z., Niu, F., Huang, W., Lu, P., Feng, E., and Han, H.: Thermal diffusivity of
556   thermokarst lake ice in the Beiluhe basin of the Qinghai-Tibet Plateau, Ann. Glaciol., 55(66),
557   153-158, 2014.

558 Su, F., Zhang, L., Ou, T., Chen, D., Yao, T., Tong, K., and Qi, Y.: Hydrological response to future
559   climate changes for the major upstream river basins in the Tibetan Plateau, Global Planet.
560   Change, 136, 82-95, 2016.

561 Tian, B., Li, Z., Engram, M. J., Niu, F., Tang, P., Zou, P., and Xu, J.: Characterizing C-band
562   backscattering from thermokarst lake ice on the Qinghai-Tibet Plateau, ISPRS J. Photogramm.
563   Remote Sens., 104, 63-76, 2015.

564 Venäläinen, A., Tuomenvirta, H., Pirinen, P., Drebs A.: A Basic Finnish Climate Data Set
565   1961-2000 – Description and Illustrations. Finnish Meteorological Institute Reports 5, 2005.

566 Vesala, T., Houtari, J., Rannik, U., Suni, T., Smolander, S., Sogachev, A., Launiainen, S., and Ojala,
567   A.: Eddy covariance measurements of carbon exchange and latent and sensible heat fluxes
568   over a boreal lake for a full open-water period, J. Geophys. Res., 111, D11101, doi:
569   10.1029/2005JD006365, 2006.

570 Wang, B., Ma, Y., Chen, X., Ma, W., Su, Z., and Menenti, M.: Observation and simulation of
571   lake-air heat and water transfer processes in a high-altitude shallow lake on the Tibetan Plateau,
572   J. Geophys. Res., 120, 12327-12344, 2015.

573 Wen, L., Lyu, S., Kirillin, G., Li, Z., and Zhao, L.: Air-lake boundary layer and performance of a
574   simple lake parameterization scheme over the Tibetan highlands, Tellus A, 68, 31091,
575   doi:10.3402/tellusa.v68.31091, 2016.

576 Wen, L., Lyu, S., Li, Z., Zhao, L., and Nagabhatla, N.: Impacts of the two biggest lakes on local
577   temperature and precipitation in the Yellow River Source Region of the Tibetan Plateau, Adv.
578   Meteorol., 2015, 248031, doi:10.1155/2015/248031, 2015.

579 Wright, D.M., Posselt, D.J., and Steiner, A.L.: Sensitivity of lake-effect snowfall to lake ice cover
580   and temperature in the Great Lakes region, Mon. Weather Rev., 141, 670-689, 2013.

581 Wu, G., Duan, A., Liu, Y., Mao, J., Ren, R., Bao, Q., He, B., Liu, B., and Hu, W.: Tibetan Plateau
582   climate dynamics: recent research progress and outlook, Natl. Sci. Rev., 2, 100-116, , 2015.

583 Wu, Q., Zhang, P., Jiang, G., Yang, Y., Deng, Y., and Wang, X.: Bubble emissions from
584   thermokarst lakes in the Qinghai-Xizang Plateau, Quatern. Int., 321, 65-70, 2014.

585 Yang, K., Ye, B., Zhou, D., Foken, T., Qin, J., and Zhou, Z.: Response of hydrological cycle to
586   recent climate changes in Tibetan Plateau, Climatic Change, 109, 517-534, 2011.

587 Yang, Y., Cheng, B., Kourzeneva, E., Semmler, T., Rontu, L., Leppäranta, M., Shirasawa, K., and
588   Li, Z.: Modelling experiments on air–snow–ice interactions over Kilpisjärvi, a lake in northern
589   Finland, Boreal Env. Res., 18(5), 341–358, 2013.
590 Yang, Y., Leppäranta, M., Cheng, B., Heil, P., Li, Z.: Numerical modeling of snow and ice
591   thickness in Lake Vanajärvesi, Finland, Tellus A, 64, 17202, doi:10.3402/tellusa.v64i0.17202,
592   2012.
593 Zhang. G., Yao, T., Xie, H., Zhang, K., and Zhu, F.: Lakes' state and abundance across the Tibetan
594   Plateau, Chinese Sci. Bull., 59(24), 3010-3021, 2014.

Table 1. Parameters and input data applied in the model reference run

Variables	Value	Source
V_a, T_a, Rh, Q_s, Q_l	Time series	Observations at BWS
Ice density ρ_i	900 kg m^{-3}	Huang et al. (2012, 2013)
Thermal conductivity k_i	1.80 W m^{-1} K^{-1}	Huang et al. (2013)
Albedo α	0.1- 0.55	Briegleb et al. (2004)
Ice extinction coefficient κ_i	(1.5–17) m^{-1}	Launiainen and Cheng (1998) adapted from Grenfell and Maykut (1977)
Bottom heat flux F_w	Time series	Parameterized based on in-ice temperature profile and ice bottom growth rate (Huang et al., to be submitted)
Initial ice thickness	0.05 m	Observation
Initial ice temperature	Linear interpolation between T_a and T_b	Calculation

Table 2. The mean bias error (*MBE*), mean absolute error (*MAE*), standard deviation (*STD*), root mean square error (*RMSE*), and correlation coefficient (*R*) between modeled and observed ice mass balance components with *n*=4023 (in cm)

Items	Surface height	Bottom height	Ice thickness
MBE	0.2	4.2	4.1
MAE	2.5	4.8	4.3
STD	2.9	3.6	3.0
RMSE	2.9	5.5	5.0
R	0.97	0.99	0.99

Table 3. The monthly means of heat fluxes (in W m^{-2}) within the air-ice-water column. Q_s: incident solar radiation; Q_{sn}: net solar radiation; Q_{ss}: net solar radiation for surface heat balance; Q_{ln}: net longwave radiation; Q_h: sensible heat flux; Q_{le}: latent heat flux; F_c: surface conductive heat flux; F_m: net surface heat flux, that is, the sum of Q_{ss}, Q_{ln}, Q_h, Q_{le} and F_c; Q_{si}: solar radiation absorption within the ice interior; Q_{sw}: solar radiation into under-ice water; F_w: heat flux from water into ice.

Month	11	12	1	2	3	4
Q_s	162	142	138	176	208	259
Q_{sn}	110	69	63	110	135	169
Q_{ss}	37	30	32	57	65	62
Q_{ln}	-112	-100	-83	-87	-79	-73
Q_h	-10	15	15	17	-1	4
Q_{le}	-46	-31	-32	-54	-53	-53
F_c	125	85	68	68	69	63
F_m	-6	-0.1	0.1	0.2	2	4
Q_{si}	35	26	23	40	49	63
Q_{sw}	39	14	8	14	21	43
F_w	34	21	20	20	21	36

Table 4. Comparisons of lake and meteorological features between Lake BLH-A and an Arctic lake (Lake Orajärvi)

Items	Lake BLH-A	Lake Orajärvi**
Surface area	0.015 km^2	11 km^2
Mean depth	2.5 m	4.4 m
Altitude	4600 m	182 m
Annual precipitation	353 mm	500 mm
Annual evaporation	1613 mm	450 mm (Venäläinen et al., 2005)
Air temperature*	-10.6 ℃	-9~-10 ℃
Wind speed*	6.5 m s^{-1}	2.3 m s^{-1}
Relative humidity*	34%	85%~87%
Short-wave radiation*	390 W m^{-2}	41-46 W m^{-2}
Long-wave radiation*	180 W m^{-2}	240-260 W m^{-2}
Net long-wave radiation*	-89 W m^{-2}	-19~-27 W m^{-2}
Snow cover	Negligible (light dust)	Up to over 30 cm
Ice surface sublimation	30 cm	Negligible
Ice structure	Congelation ice	Snow-ice + superimposed ice + congelation ice

*averaged over whole ice season

**data during winters of 2010-2012 were used for statistics
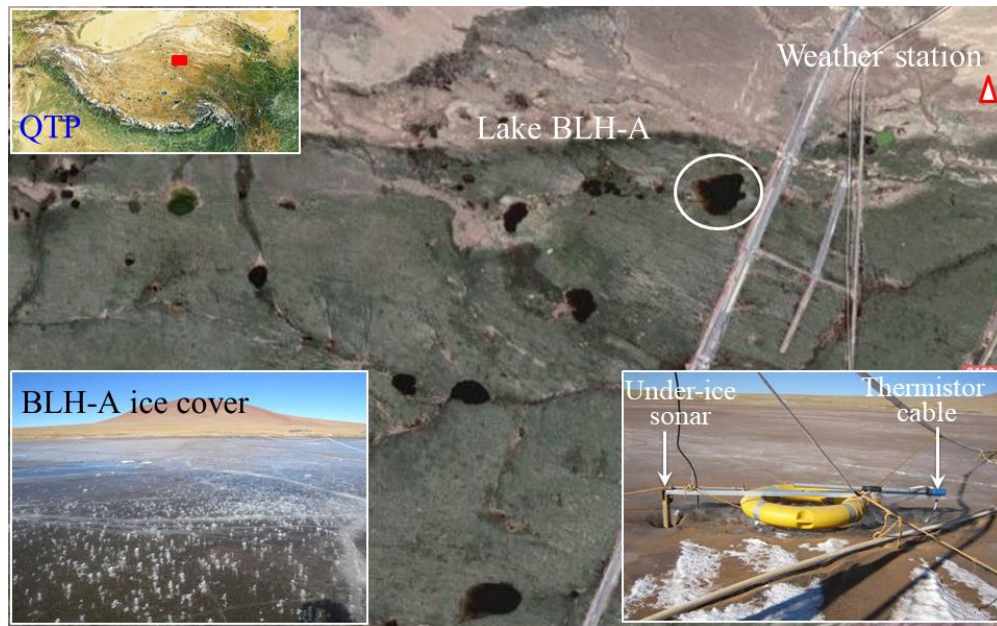
Figure 1. Location of Lake BLH-A. The lower left insert photo shows the lake ice cover including numerous large bubbles, while the lower right insert shows field instrumentation for temperature and ice thickness measurements. Thin deposited find sand film (dark yellow) is also seen in both inserts.
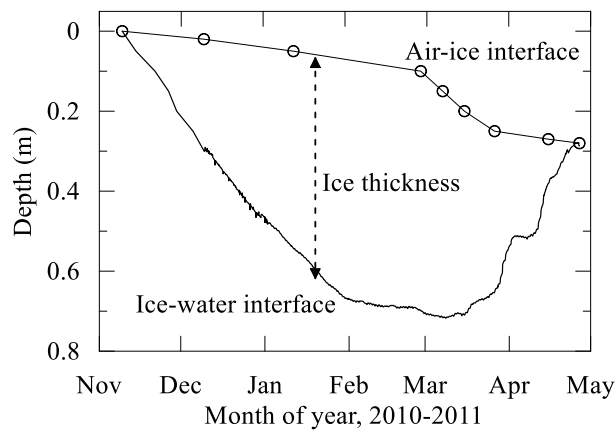
Figure 2. The observed lake ice thickness evolution over the whole 2010–2011 ice season. The open circles denote the observed location of the ice surface, and the solid lines connecting the circles denote the linear interpolation.
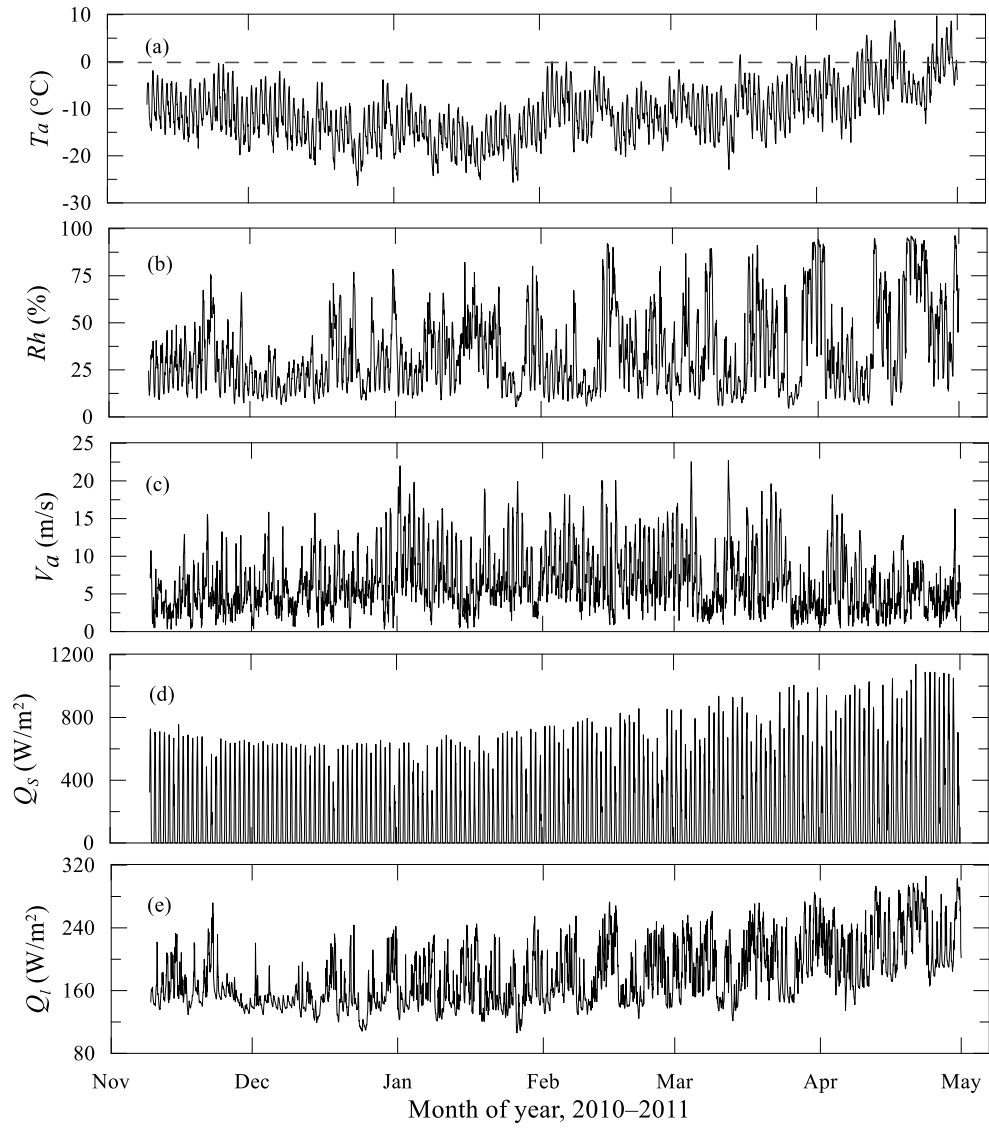
Figure 3. The time series of observed meteorological variables through the whole ice season of 2010–2011. (a) daily mean air temperature T_a, (b) relative humidity Rh, (c) wind speed V_a, (d) incident shortwave solar radiation Q_s, and (e) incident longwave radiation Q_l.
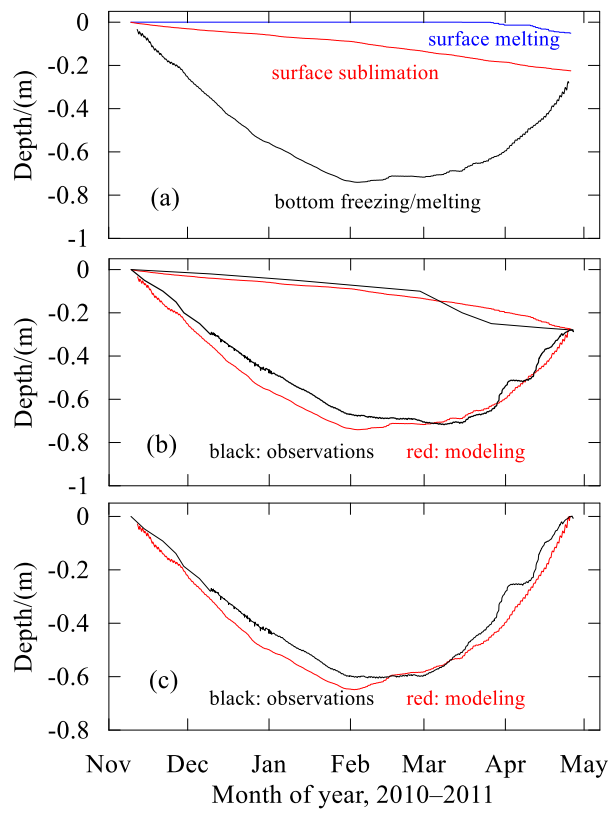
Figure 4. The HIGHTSI modeled BLH lake ice mass balance components (a), the ice surface and bottom evolution (b), and the ice thickness (c).
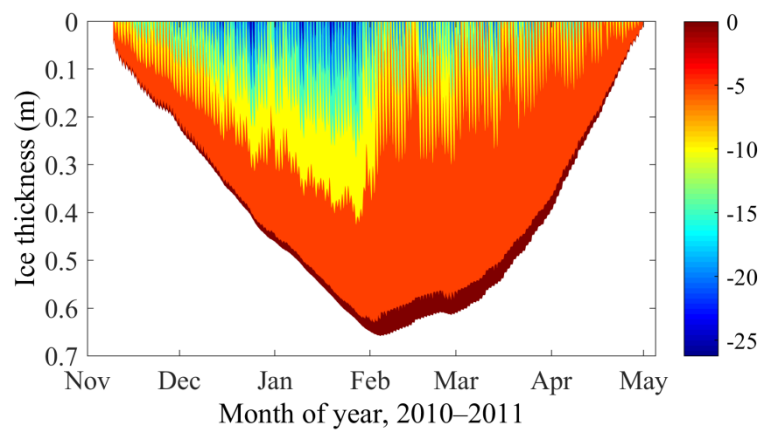
Figure 5. HIGHTSI modeled ice temperature regime for winter 2010–2011.
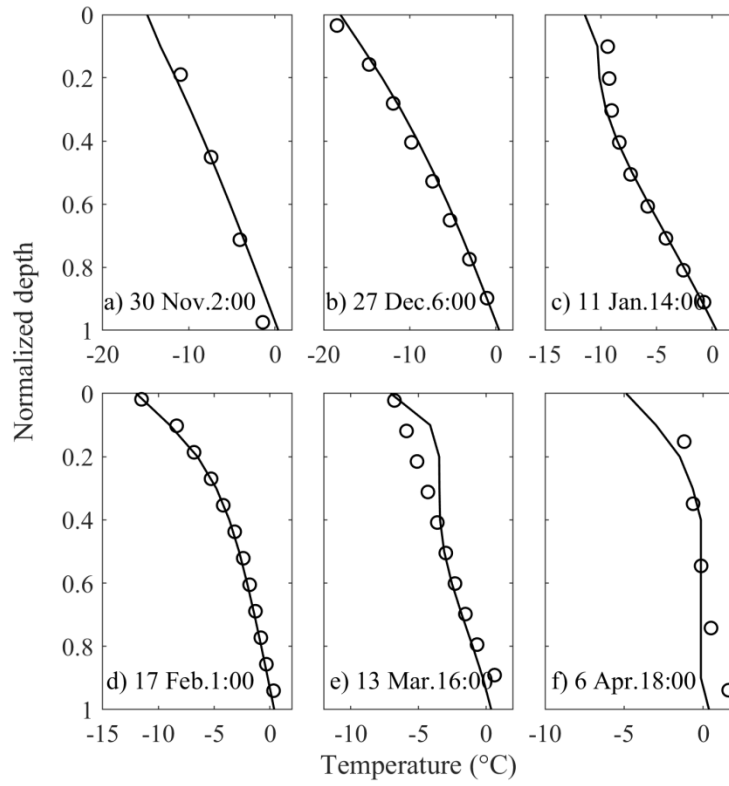
Figure 6. Comparisons of modeled (lines) and observed (circles) vertical temperature profiles of within ice at selected time steps. A normalized depth (depth divided by ice thickness) is used as the y-axis (0 and 1 denote the ice surface and bottom, respectively).
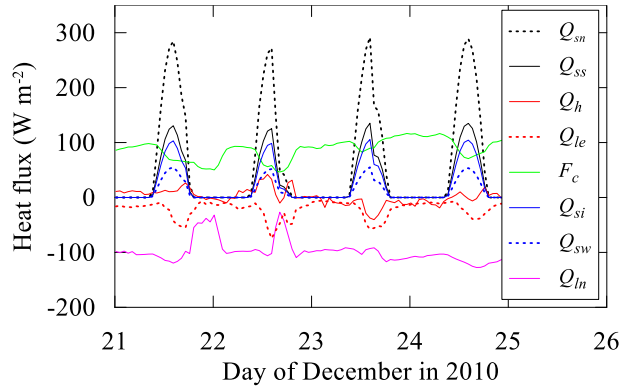
Figure 7. Diurnal patterns of various radiation/heat fluxes
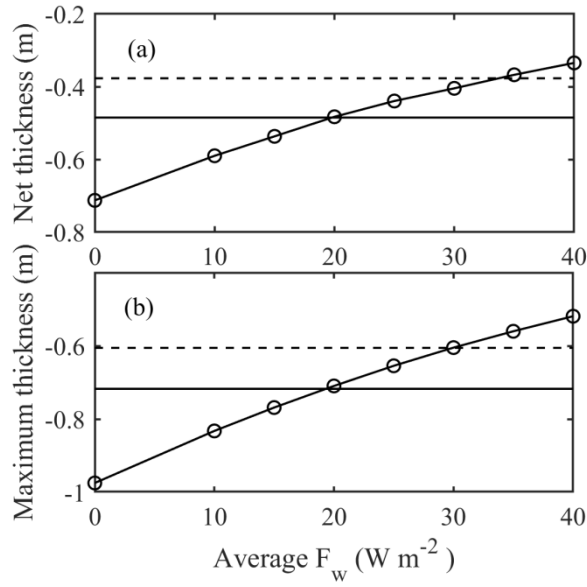
Figure 8. Modeled (lines with circles) average (a) and maximum (b) ice thickness applying different constant F_w. The broken lines are observed average and maximum ice thickness during the simulation period. The solid lines are observed average and maximum ice growth at ice bottom.
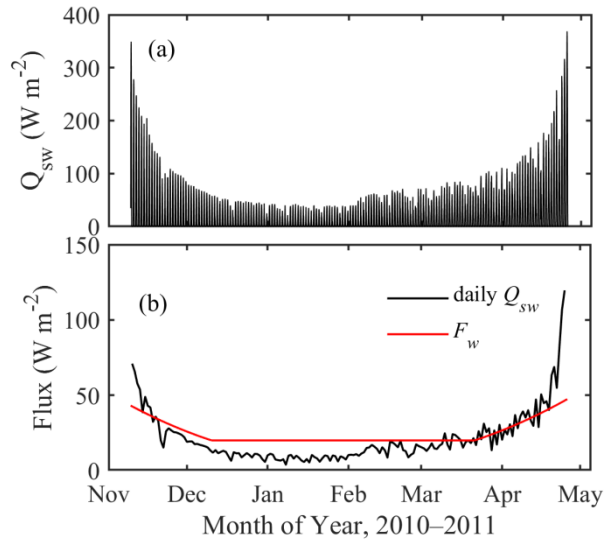
Figure 9. Modeled solar radiation penetration (Q_{sw}) into the under-ice water column: hourly (a) and daily averages (b) with prescribed F_w during the simulation period.
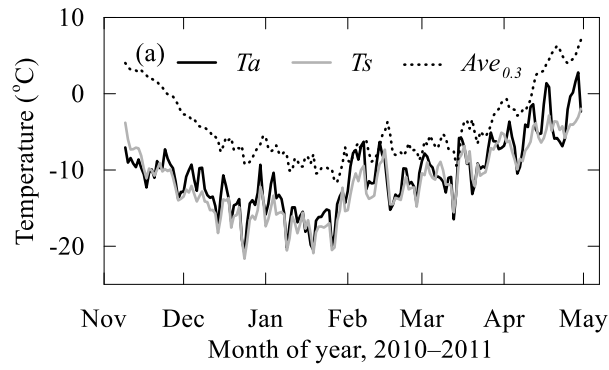
Figure 10. Daily means of the observed air temperature (T_a), the averaged ice/water temperature of the top 30 cm ($Ave_{0-0.3}$), and the calculated ice surface temperature (T_s).
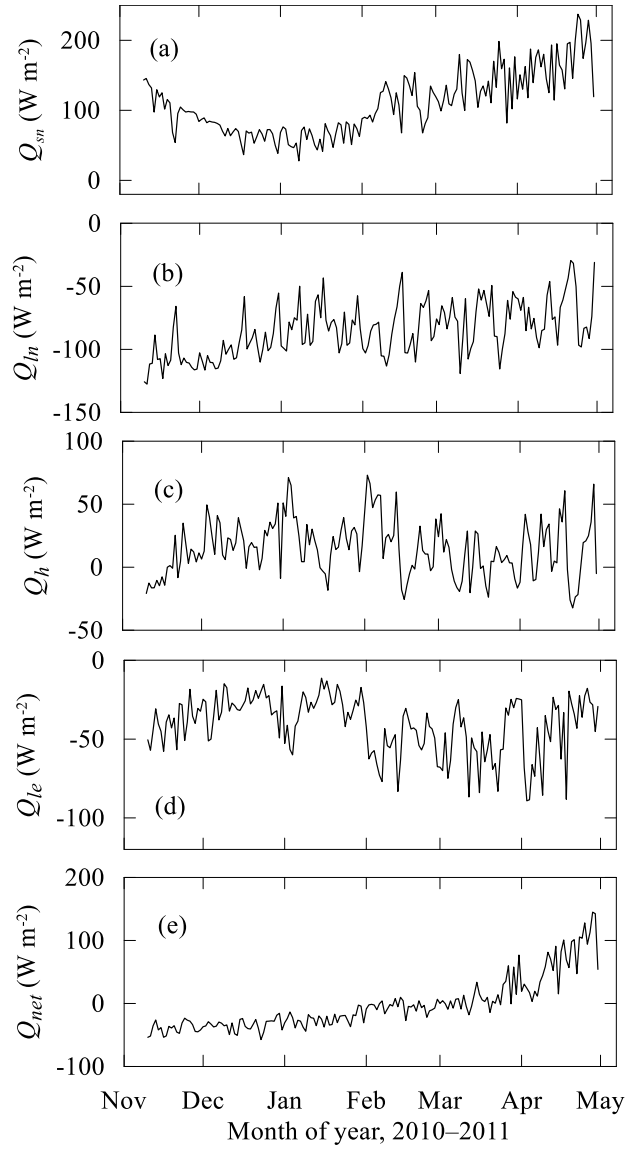
Figure 11. Daily means of the surface energy balance components of net shortwave (Q_{sn}) and longwave (Q_{ln}) radiation, turbulent sensible (Q_h) and latent (Q_e) heat fluxes, and net flux into the lake ($Q_{net}= Q_{sn}+Q_{ln}+Q_h+Q_{le}$) though the entire ice season.
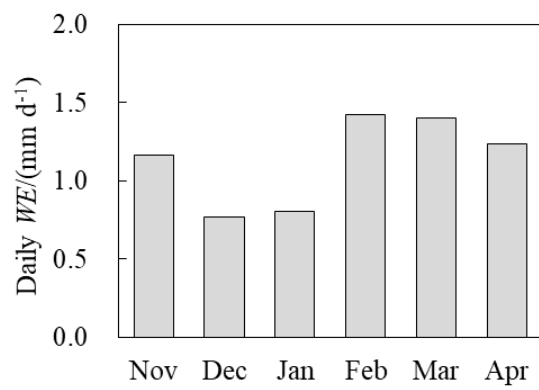
Figure 12. The daily mean surface sublimated water equivalent (*WE*) through the winter 2010–2011.